

Terahertz Near-Field Vortex Beams with Variable Intensity Profiles Based on Geometric Metasurfaces

Yang Zhu, Yiwen Zhou, Zhiyuan Fan, Xiaofei Zang,* Yiming Zhu,*
and Songlin Zhuang

Electromagnetic waves possessing orbital angular momentum, namely, vortex beams, have attracted considerable attention in the fields ranging from optical communications to quantum science, due to their extraordinary information encoding capabilities. Vortex beams are traditionally exhibited with a doughnut-shaped intensity distribution, where a null intensity center surrounded by a bright ring, caused by the phase singularity. Herein, geometric metasurface devices that can generate near-field vortex beams with variable intensity profiles are proposed and experimentally demonstrated. The generation of a vortex beam with tailored intensity profile is realized by integrating the azimuthal nonlinear phase and spiral phase into ring-shaped anisotropic air-slit arrays. As proof-of-principle examples, multiple geometric metasurfaces that generate vortex beams with C_N -fold rotational symmetric or asymmetric intensity profiles in the near-field are demonstrated in the terahertz domain. This unique capability for terahertz near-field vortices with variable intensity distributions based on geometric metasurface approach opens an avenue to develop multifunctional integrated systems and system-on-chip devices, leading to potential applications in microscopy, integrated photonics, quantum information processing, and optical communication.

the topological charge (l), which is originated from the azimuthal angle-dependent phase profile defined as $\exp(i l \varphi)$. Intrinsically, the OAM of electromagnetic (EM) waves has infinite number of eigen modes, which makes it a great candidate for applications of high-capacity data transmission and communication.^[3,4] Due to the special phase profile and the phase singularity, vortex beams have also been applied in particle manipulation and quantum exploration.^[5–7] On the other hand, the traditional vortex beam is always exhibited with a doughnut-shaped intensity profile, that is, a null intensity center surrounded by a bright ring with $O(2)$ continuous rotational symmetry. Indeed, when transforming the phase singularity with $O(2)$ continuous rotational symmetry into C_N -fold discrete rotational symmetry, vortex beams with variable intensity distributions can be generated.^[8–10] Conventional approaches using the polygonal lenses or spatial light modulators as the diffractive elements have been proposed and demon-

strated to generate vortex beams with the intensity profiles featuring C_N -fold discrete rotational symmetry. However, these traditional diffractive elements are limited to the bulk size and material dispersion, which inevitably degrades their system-on-chip (SOC) and integrating implementations.


Metasurfaces, also known as the 2D metamaterials, provide an ultracompact platform to precisely manipulate the properties of EM waves at will.^[11,12] Especially, geometric metasurfaces consisting of anisotropic meta-atoms with identical shape but different in-plane orientations are one of the well-studied metasurfaces, which can locally tailor the amplitude, phase, and polarization of EM waves at subwavelength resolution.^[13] By carefully designing the orientation of each anisotropic meta-atom, the required phase profile can be produced by a geometric metasurface, enabling the control of the wave front of EM waves. Recent works regarding geometric metasurfaces such as generalized Snell's law,^[14–16] holograms,^[17–24] metalens,^[25–34] spin Hall effect,^[35–38] polarization convertors,^[39–43] and nonlinear photonics^[44–47] have sufficiently proven their outstanding capabilities in EM wave manipulation. Moreover, the generations of vortex beams,^[48–52] vector vortex beams,^[53,54] and perfect vortex beams^[55–57] have been demonstrated using geometric metasurface approach. Recently, generalized vortex beams, in

1. Introduction

Vortex beams carrying orbital angular momentum (OAM) naturally exhibit two typical characteristics: the helical/twisted wave fronts and doughnut-shaped intensity profiles.^[1,2] On one hand, the degree-of-freedom of helicity is dependent on

Y. Zhu, Y. Zhou, Z. Fan, X. Zang, Y. Zhu, S. Zhuang
Terahertz Technology Innovation Research Institute, and Shanghai Key
Lab of Modern Optical System
University of Shanghai for Science and Technology
No. 516 JunGong Road, 200093 Shanghai, China
E-mail: xfzang@usst.edu.cn; ymzhu@usst.edu.cn

X. Zang, Y. Zhu
Shanghai Institute of Intelligent Science and Technology
Tongji University
20092, China

 The ORCID identification number(s) for the author(s) of this article can be found under <https://doi.org/10.1002/adpr.202200151>.

© 2022 The Authors. Advanced Photonics Research published by Wiley-VCH GmbH. This is an open access article under the terms of the Creative Commons Attribution License, which permits use, distribution and reproduction in any medium, provided the original work is properly cited.

DOI: 10.1002/adpr.202200151

which the corresponding intensity profiles have C_N -fold discrete rotational symmetry instead of continuous rotational symmetry for conventional vortices, have been realized in free space, extending the study of vortex beam and providing a new perspective on controlling the properties of EM waves.^[58,59] However, these previous studies focus on the vortex with variable intensity profiles in the far field, and the intensity profiles of these generalized vortices are limited to the C_N -fold discrete rotational symmetry. Near-field vortices (that are surface plasmonic vortices) generated by metal-based structures enable an unprecedented capability in confining, manipulating, and enhancing EM fields at subwavelength mode volumes, and thus, they open a new avenue to significantly reduce the vortex size that can be applied in integrated nanophotonics.^[60–62] However, the near-field vortex with a variable intensity distribution, and in particular, the vortex with an asymmetric intensity profile, has not been well explored so far because the plasmonic vortex with transformable intensity profile provides a generalized spatial dimension in trapping and manipulating microparticles.

In this article, we investigate the excitation of near-field terahertz (THz) OAM with a variable intensity profile based on geometric metasurface. Functionalities featuring of simultaneously generating near-field vortex beams and manipulating the corresponding intensity profiles are realized by integrating the azimuthal nonlinear phase and spiral phase into geometric metasurfaces consisting of ring-shaped anisotropic slits with predesigned orientations. In experiment, we demonstrate the generation of near-field vortex beams with C_N -fold rotational symmetric, i.e., C_{3-} , C_{4-} , and C_{5-} fold rotational symmetric, and asymmetric (e.g., vortex beam with arbitrary shape) intensity distributions using geometric metasurfaces encoded with the required phase profiles. The demonstrated metasurface approach for generating near-field THz vortex beams with variable intensity profiles will enable various applications in manipulating particles, SOC, and optical tweezers, to name a few.

2. Principle and Design

Figure 1 schematically shows a geometric metasurface that can transfer the incident THz waves (a Gaussian THz beam) into a near-field vortex with a predesigned topological charge and a variable intensity profile. Such a geometric metasurface consists of air-slit arrays etched in an ultrathin gold film deposited on a polyimide (PI with $\epsilon_{PI} = 3.5 + 0.035i$) substrate. By integrating a spiral phase (that is phase to generate the traditional vortex with a null intensity center surrounded by a bright ring) and an extra azimuthal nonlinear phase (to transfer the traditional vortex into a vortex with a variable intensity profile) into the geometric metasurface, the excited THz surface waves with a position-dependent phase from each air-slit can be formed into a vortex with a variable intensity profile under the illumination of circularly polarized (CP) THz waves. The spiral phase is designed to convert the excited surface waves into a near-field vortex, while the azimuthal nonlinear phase enables the functionality in reshaping the corresponding intensity profile. By carefully designing the orientation of each air-slit, one can accurately control the topological charge and intensity distribution of the near-field vortex.

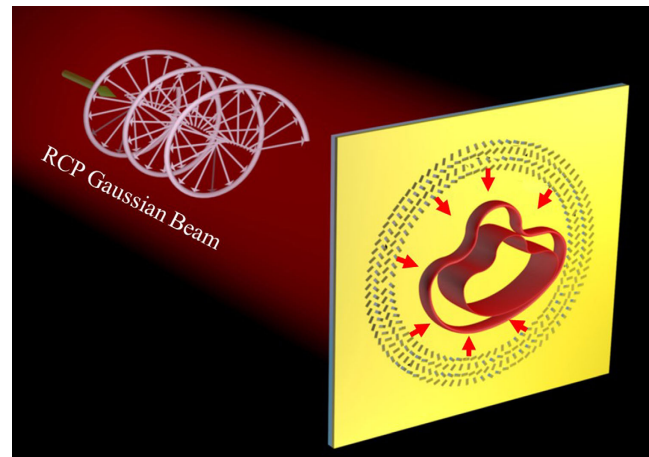


Figure 1. Schematic of the geometric metasurface for generating near-field vortex with variable intensity profile: the ring-shaped geometric metasurface consists of air-slit arrays with predesigned orientations. For the incidence of RCP THz waves, the designed geometric metasurface allows to excite the surface waves into a near-field vortex with variable intensity profile.

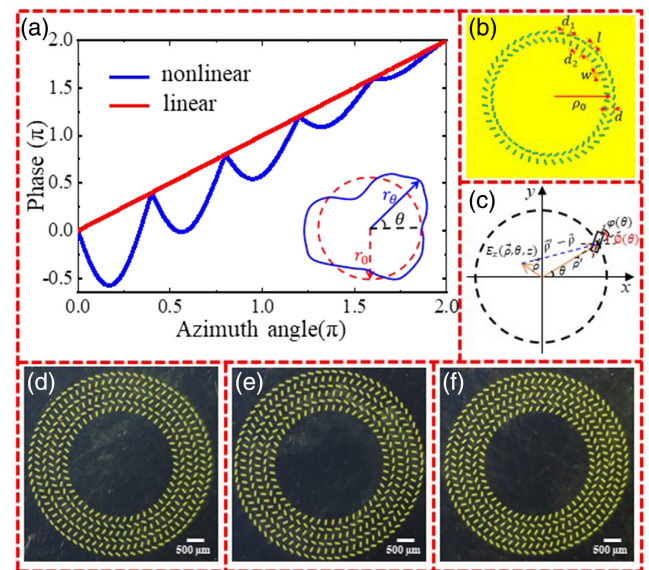


Figure 2. The schematics of the fundamental principle and the fabricated samples of the designed geometric metasurfaces. a) The linear (red) and nonlinear vortex phase profiles along the azimuthal direction. b) The designed structure of a geometric metasurface for generating near-field vortex with variable intensity profiles. c) Schematic of an air-slit for exciting surface waves. d–f) The optical images of the samples for, respectively, generating near-field vortices with C_{3-} and C_{4-} fold rotational symmetric, or asymmetric intensity profiles. Inset in (a) is the schematic of the vortices under the modulations of linear (red) and linear combined with nonlinear vortex phase (blue).

The comparison of the traditional vortex and generalized vortex with the corresponding phase structures is schematically shown in **Figure 2a**. For the traditional canonical vortex that contains a null intensity center surrounded by a bright ring due to the phase singularity (see the red curve in **Figure 2a**), whereas the helical phase profile exhibits a linearly increased phase in the

azimuthal direction. While in terms of noncanonical/generalized vortex with a variable intensity profile (see the blue curve of insets in Figure 2a), an extra azimuthal nonlinear phase is added into the traditional spiral phase (a linearly increased phase) to manipulate the intensity profile, meanwhile preserving the topological charge. As an anisotropic air-slit on a metal-based film can excite surface waves with a tailored phase,^[63] the near-field vortex with a nonlinear phase profile can be obtained by locally tailoring the orientation angle of each air-slit, as shown in Figure 2b. The optimized structure parameters of the ring-shaped metasurfaces are $l = 210 \mu\text{m}$, $w = 60 \mu\text{m}$, $\lambda_{\text{SPP}} = \lambda_0 \sqrt{\frac{\epsilon_d + \epsilon_m}{\epsilon_d \epsilon_m}}$ (the wavelength of surface wave, λ_0 , is the wavelength of the incident THz waves in vacuum), $d = d_1 = d_2 \approx \lambda_{\text{SPP}}/2$, $\rho_0 = m\lambda_{\text{SPP}}$ (m is integer; ρ_0 is the distance between the center of the air-slit in the innermost ring and the origin of coordinates). The working wavelength of THz waves is $\lambda = 600 \mu\text{m}$. ϵ_m and ϵ_d are the permittivity of metal and dielectric, respectively.

For an air-slit embedded in the gold film (see Figure 2c), the excited surface waves under the illumination of CP EM waves can be expressed as

$$E_z = e^{-\alpha z} A(\theta) e^{\pm i\phi(\theta)} e^{ik_{\text{SPP}}|\vec{\rho}-\vec{\rho}'|} e^{-\beta|\vec{\rho}-\vec{\rho}'|} \quad (1)$$

where $A(\theta) = A_0 \cos(\varphi(\theta))$ is the amplitude of a dipole source and $\varphi(\theta) = \phi(\theta) - \theta$. \pm is determined by the right-handed circularly polarized (RCP) and left-handed circularly polarized (LCP) incidence. ρ is the distance between a field point and the origin of coordinates, while ρ' is the distance between the center of each slit and the origin of coordinates. α and β are attenuation coefficients in the z direction and the propagation direction (of the near-field vortex), respectively. The detailed discussion of the attenuation term (β) along the propagation direction is given in Section S1, Supporting Information.

When a single-ring structured air-slit array is designed, and each air-slit has a special rotation angle $\phi(\theta)$, the excited surface waves can be described as

$$E_z = e^{-\alpha z} \int A(\theta) e^{\pm i\phi(\theta)} e^{ik_{\text{SPP}}|\vec{\rho}-\vec{\rho}'|} e^{-\beta|\vec{\rho}-\vec{\rho}'|} d\theta \quad (2)$$

To avoid the spin-assisted OAM number,^[64] a dual-ring air-slit array (see Figure 2b) with each unit cell containing a pair of orthogonally distributed air-slits is employed to control the THz near-field OAM with variable intensity profiles. For the incidence of CP THz waves, the electric-field distribution of the dual-ring air-slit array is governed as

$$E_z = e^{-\alpha z} \int (A_{\text{in}}(\theta) e^{\pm i\phi(\theta)} + A_{\text{out}}(\theta) e^{\pm i(\phi(\theta) + \frac{\pi}{2})}) e^{ik_{\text{SPP}}d} \times e^{ik_{\text{SPP}}|\vec{\rho}-\vec{\rho}'|} e^{-\beta|\vec{\rho}-\vec{\rho}'|} d\theta \quad (3)$$

where d is the distance between the inner and outer rings. If $\phi(\theta) = n\theta$ (a linearly increased phase), then $A_{\text{in}}(\theta) = A_0 \cos((n-1)\theta)$, $A_{\text{out}}(\theta) = A_0 \cos((n-1)\theta + \frac{\pi}{2})$. When $d = \lambda_{\text{SPP}}/2$, Equation (3) can be rewritten as

$$\begin{aligned} E_z &= e^{-\alpha z} \int (A_{\text{in}}(\theta) e^{\pm i\phi(\theta)} + A_{\text{out}}(\theta) e^{\pm i(\phi(\theta) + \frac{\pi}{2})}) e^{ik_{\text{SPP}}\frac{\lambda_{\text{SPP}}}{2}} \\ &\quad \times e^{ik_{\text{SPP}}|\vec{\rho}-\vec{\rho}'|} e^{-\beta|\vec{\rho}-\vec{\rho}'|} d\theta \\ &= e^{-\alpha z} \int A_0 (\cos(n-1)\theta \pm i \sin(n-1)\theta) \\ &\quad \times e^{\pm in\theta} e^{ik_{\text{SPP}}|\vec{\rho}-\vec{\rho}'|} e^{-\beta|\vec{\rho}-\vec{\rho}'|} d\theta \\ &= e^{-\alpha z} \int A_0 e^{\pm i(2n-1)\theta} e^{ik_{\text{SPP}}|\vec{\rho}-\vec{\rho}'|} e^{-\beta|\vec{\rho}-\vec{\rho}'|} d\theta \\ &\propto J_{\pm(2n-1)}(k_{\text{SPP}}\rho) \end{aligned} \quad (4)$$

where J is the Bessel function. We set $n=1$, and thus, the topological charge of the generated near-field vortex (with a ring-shaped intensity profile) is ± 1 . The initial rotation angles (at $\theta=0^\circ$) of air slits in the inner and outer rings are $\pi/2$ and 0 , respectively.

In order to generate a THz near-field vortex beam with a variable intensity profile, a nonlinear phase should be introduced in the geometric metasurface

$$\kappa(\theta) = \arg \left\{ \exp \left[i \frac{2\pi}{\lambda_{\text{SPP}}} \left((\vec{\rho}' \cos(\theta) - (r_\theta - r_0) \cos(\theta))^2 + (\vec{\rho}' \sin(\theta) - (r_\theta - r_0) \sin(\theta))^2 \right) \right] \right\} \quad (5)$$

where r_0 is the constant that represents the radius of the traditional vortex without a variable intensity profile (or the radius of the traditional vortex without the modulation of nonlinear phase in Equation (5)) and r_θ is the azimuthal-dependent radius of the vortex with a variable intensity profile (see inset in Figure 2a). By embedding such a nonlinear phase into our designed metasurface, the electric-field distribution in Equation (4) is modulated as

$$\begin{aligned} E_z &= e^{-\alpha z} \int (A_{\text{in}}(\theta) e^{\pm i(n\theta + \kappa(\theta))} + A_{\text{out}}(\theta) e^{\pm i(n\theta + \kappa(\theta) + \frac{\pi}{2})}) \\ &\quad \times e^{\pm i\kappa(\theta)} e^{ik_{\text{SPP}}\frac{\lambda_{\text{SPP}}}{2}} e^{ik_{\text{SPP}}|\vec{\rho}-\vec{\rho}'|} e^{-\beta|\vec{\rho}-\vec{\rho}'|} d\theta \\ &= e^{-\alpha z} \int A_0 (\cos(n-1)\theta \pm i \sin(n-1)\theta) \\ &\quad \times e^{\pm in\theta} e^{\pm i\kappa(\theta)} e^{ik_{\text{SPP}}|\vec{\rho}-\vec{\rho}'|} e^{-\beta|\vec{\rho}-\vec{\rho}'|} d\theta \\ &= e^{-\alpha z} \int A_0 e^{\pm i(2n-1)\theta} e^{\pm i\kappa(\theta)} e^{ik_{\text{SPP}}|\vec{\rho}-\vec{\rho}'|} e^{-\beta|\vec{\rho}-\vec{\rho}'|} d\theta \\ &\propto J_{\pm(2n-1)}(k_{\text{SPP}}\rho_\theta) \end{aligned} \quad (6)$$

Therefore, the rotation angles of the air slits in the inner and outer rings are $\phi_{\text{inner}}(\theta) = \kappa(\theta) + n\theta$ and $\phi_{\text{outer}}(\theta) = \kappa(\theta) + n\theta + \pi/2$, respectively.

For example, by breaking the traditional vortex with $O(2)$ continuous symmetry into C_N discrete rotational symmetry, the required structure parameter is governed as

$$r_\theta = \frac{r_0}{\cos(\frac{\pi}{N} - \text{mod}(\theta, \frac{2\pi}{N}))} \quad (7)$$

To obtain a near-field vortex with an asymmetric intensity profile, the structure parameter can be written as

$$r_\theta = r_0 \left\{ 1 + A(\theta) \sin \left[2 \left(\theta - \frac{\pi}{4} \right) \right] \right\} \quad (8)$$

where $A(\theta)$ is an azimuthal-dependent parameter and $A(\theta) \in [0, 1]$.

3. Results

To verify the proposed method, we first design a geometric metasurface (see Figure 2d) that can convert the incident THz waves into surface waves and simultaneously gather into a near-field vortex with C_3 discrete rotational symmetry propagating along the interface between air and metal, as shown in Figure 3. The designed structure parameter for generating a near-field vortex with triangle-shaped intensity profile is set to be $r_\theta = r_0 / (\cos(\frac{\pi}{3} - \text{mod}(\theta, \frac{2\pi}{3})))$, where $\theta \in [0, 2\pi]$. The analytical electric field intensity ($|E_z|^2$) and phase distributions of the predesigned vortex are shown in Figure 3a₁,a₂, respectively. The vortex beam with a dark region in the center surrounded by a triangle-shaped intensity profile is observed, as shown in Figure 3a₁ (also see the black-dotted box). Such a noncanonical vortex is located at (0, 0), and the corresponding phase distribution (see the white-dotted box in Figure 3a₂) also exhibits a triangle-shaped profile. There is only one phase jump from $-\pi$ to π , indicating that a vortex beam with a topological charge of +1 is preserved after the modulation of a triangle-shaped phase. Furthermore, by encoding such a singular phase (triangle-shaped phase) via accurately tailoring the orientation of each air-slit, such a near-field vortex with the predesigned intensity profile can be realized (see both numerically simulated and experimentally measured results in Figure 3b₁–c₂). Finite element method (FEM) is applied to numerically simulate the electric-field intensity and phase distributions of the resultant near-field vortex from metasurfaces. As can be seen from Figure 3b₁, under the illumination of RCP THz waves, the simulated electric field intensity distribution indeed exhibits a triangle-shaped

hollow ring, demonstrating the symmetry breaking from $O(2)$ continuous symmetry into C_3 -fold discrete rotational symmetry. The phase distribution shown in Figure 3b₂ also presents a triangle-shaped profile as expected. Experimentally, a near-field scanning THz time-domain spectrum microscopy system (see the experimental setup in Section S2, Supporting Information) is used to characterize the performance of the fabricated metasurfaces. Figure 3c₁,c₂ illustrates the measured electric field intensity and phase distributions. A triangle-shaped vortex is observed nearby the surface of the fabricated sample, as shown in Figure 3c₁ (the distance between the detecting and sample planes is about 100 μm). The measured intensity and phase in Figure 3c₁,c₂ show a triangle-shaped profile, which agree well with the analysis and FEM results except for a slight discrepancy originated from fabrication and testing errors.

To further demonstrate the versatility and robust of our proposed approach, the near-field vortex with C_4 discrete rotational symmetry is investigated and shown in Figure 4. Here, the designed structure parameter is designed as $r_\theta = r_0 / (\cos(\frac{\pi}{4} - \text{mod}(\theta, \frac{\pi}{2})))$, where $\theta \in [0, 2\pi]$. According to Equation (3), the electric field intensity of such a vortex should be exhibited as a square-shaped profile. As can be seen in Figure 4a₁ for the analysis model, the generated vortex beam enables the C_4 discrete rotational symmetry, showing a dark zone in the center surrounded by a square-shaped bright ring. The phase distribution of Figure 4a₂ also exhibits a square-shaped profile (indicated by a white-dotted box). The topological charge of the resultant EM field is still $l = 1$ for such a square-shaped vortex because the phase change is 2π around the center. When such a phase profile (with C_4 discrete rotational symmetry)

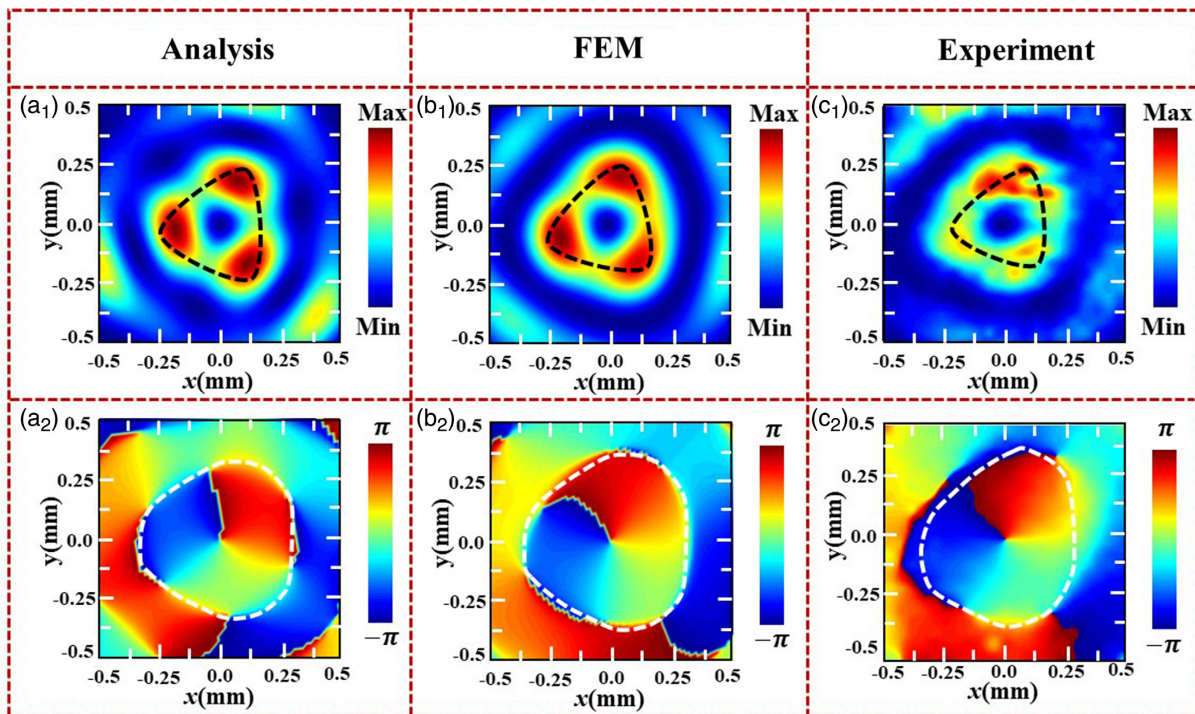


Figure 3. The electric-field intensity ($|E_z|^2$) and phase distributions of the designed geometric metasurface encoded with C_3 -fold rotational symmetric helical phase: a₁,a₂) the analysis results, b₁,b₂) the simulated results, and c₁,c₂) the measured results.

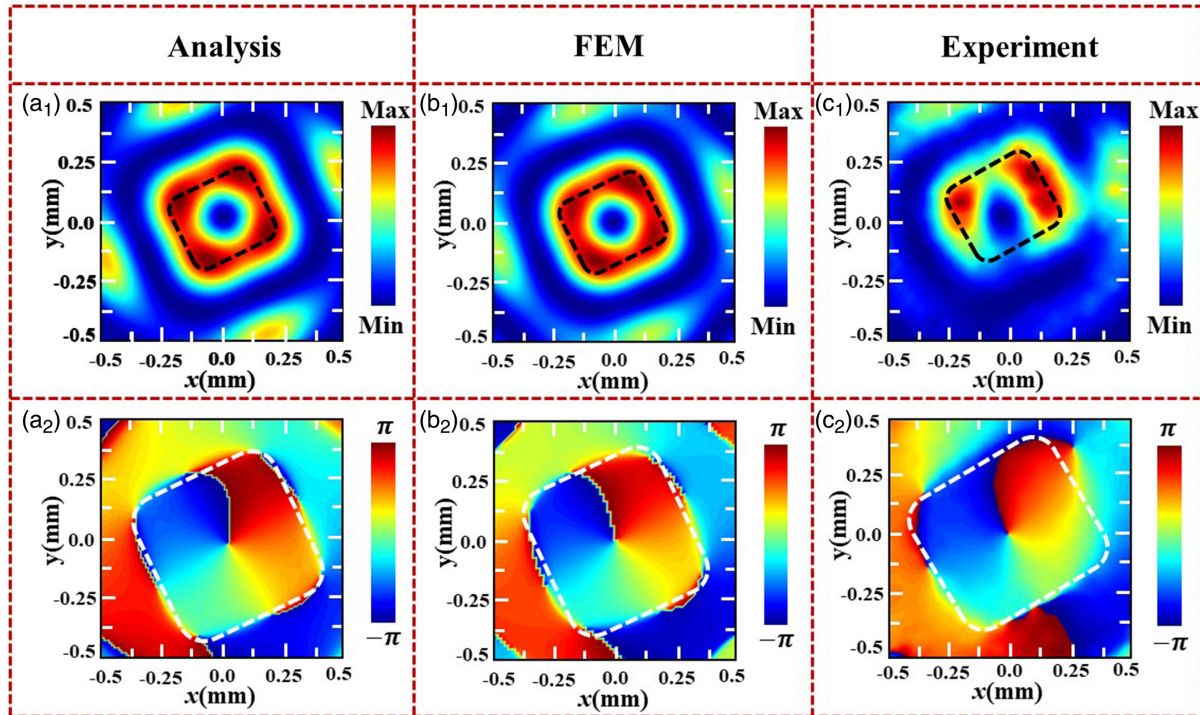


Figure 4. The electric-field intensity ($|E_z|^2$) and phase distributions of the designed geometric metasurface encoded with C_4 -fold rotational symmetric helical phase: a_1, a_2) the analysis results, b_1, b_2) the simulated results, and c_1, c_2) the measured results.

is embedded into a geometric metasurface by controlling the orientations of air-slit arrays, the near-field vortex with a square-shaped intensity profile can be generated, as shown in Figure 4 b_1 – c_2 . For the incidence of RCP THz waves, the calculated electric field intensity (see Figure 4 b_1) shows a square-shaped profile, and the corresponding phase distribution is also well matched with the intensity profile with a square-shaped configuration. Figure 4 c_1, c_2 illustrates the measured electric-field intensity and phase distributions, respectively, exhibiting the expected square-shaped hollow and solid profiles and confirming the generation of excited vortex beam with C_4 discrete rotational symmetry. The further demonstration of a geometric metasurface that can generate near-field vortex with a C_5 discrete rotational symmetry is given in Section S3, Supporting Information.

The proposed method not only allows to convert the incident THz waves into surface waves with OAM and C_N -fold rotational symmetric intensity distributions, but also enables the functionality to steer THz beam into a near-field vortex with an asymmetric intensity profile (see Figure 5). The structure parameter for generating vortex with an arbitrary intensity profile is expressed in Equation (8).

As a proof-of-concept, the structure parameter is selected as

$$r_\theta = \begin{cases} r_0 \left\{ 1 + 0.3 \sin \left[2 \left(\theta - \frac{\pi}{4} \right) \right] \right\}, & \theta \in \left(\frac{\pi}{4}, \frac{3\pi}{4} \right) \\ r_0 \left\{ 1 + 0.5 \sin \left[2 \left(\theta - \frac{3\pi}{4} \right) \right] \right\}, & \theta \in \left(\frac{3\pi}{4}, \frac{5\pi}{4} \right) \\ r_0, & \text{other} \end{cases} \quad (9)$$

According to Equation (7), two different humps should be observed at azimuthal position of $\theta = \pi/2$ and $\theta = \pi$ in the generated near-field vortex. Figure 5 a_1, a_2 illustrates the electric field intensity and phase distributions based on the analysis model. A vortex beam with one small hump at $\theta = \pi/2$ and one large hump at $\theta = \pi$ is confirmed. Moreover, the corresponding phase distribution (indicated by the white box in Figure 5 a_2) presents two humps at $\theta = \pi/2$ and $\theta = \pi$, respectively. The topological charge is still $l = 1$ because the phase change in a round is 2π . Both the electric field intensity and phase distributions with two different humps demonstrate the asymmetric characteristic of the vortex beam. The simulated electric field intensity and phase profiles (see Figure 5 b_1, b_2) also show two dissimilar humps. The experimentally measured results of such a near-field vortex with an asymmetric intensity profile are shown in Figure 5 c_1, c_2 . It is confirmed that both the measured electric field intensity (Figure 5 c_1) and phase (Figure 5 c_2) profiles present the asymmetric characteristics. The measured results are well matched with the simulated and analysis results, indicating that our proposed approach can be extended to manipulate THz near-field OAM beam with an arbitrary intensity profile.

4. Conclusion

In conclusion, we have proposed and demonstrated a flexible approach to design air-slit-based geometric metasurfaces that could transfer the incident CP THz waves into surface waves possessing OAM and variable intensity profiles. The fundamental principle for simultaneously generating near-field vortex beams

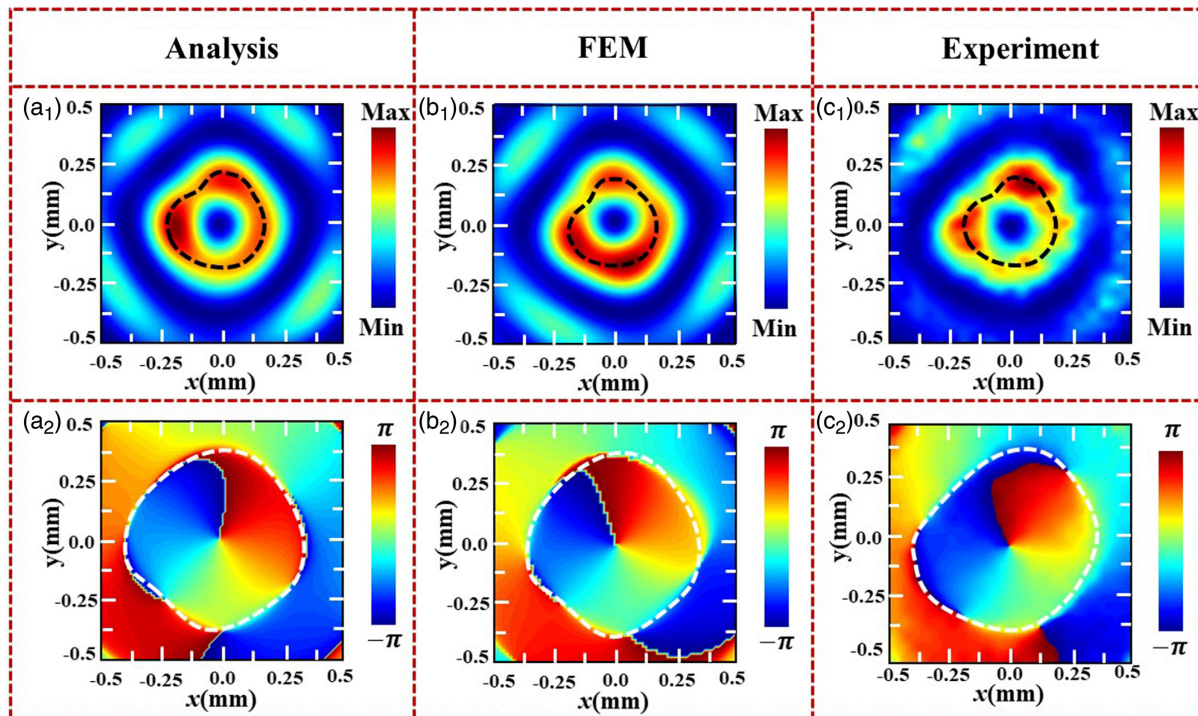


Figure 5. The electric-field intensity ($|E_z|^2$) and phase distributions of the designed geometric metasurface encoded with asymmetric helical phase: a_1, a_2) the analysis results, b_1, b_2) the simulated results, and c_1, c_2) the measured results.

and manipulating the corresponding intensity profile was constructed by integrating the nonlinear azimuthal phase and spiral phase into the geometric metasurface design. By encoding the required phase profiles into a ring-shaped array that consists of anisotropic air-slits with specific local orientations, the near-field vortices with C_N -fold rotational symmetric and asymmetric intensity profiles were demonstrated. Our unique and flexible approach for simultaneously manipulating the near-field OAM and the corresponding intensity profiles provides a unique capability to design multifunctional compact devices with potential applications in particle manipulation, information processing, and system integration.

5. Experimental Section

Sample Fabrication: Traditional photolithography and magnetron sputtering coating were used to fabricate our designed THz near-field vortex generators. The PI film was selected as the substrate, and positive resist (AZP 4620) was spin-coated (4000 rpm, 30 s) on one side of the pre-cleaned substrate. Then, the mask was used for the exposure processing. Then, 150 nm gold was deposited based on the magnetron sputtering coating. Finally, after the ultrasonic stripping, the metal-based metasurface array was formed. The experiment setup for detecting the electric field intensity and phase distributions of the fabricated samples was given in Section S1, Supporting Information.

Supporting Information

Supporting Information is available from the Wiley Online Library or from the author.

Acknowledgements

Y.Z. and Y.Z. contributed equally to this work. This work was supported in part by the National Key Research and Development Program of China (grant no. 2017YFA0701005), National Natural Science Foundation of China (grant no. 61871268), “Shuguang” Program of Shanghai Education Commission (grant no. 19SG44), Shanghai international joint laboratory project (grant no. 17590750300), and the 111 Project (grant no. D18014). The authors thank Dr. Fuyong Yue for helpful discussion.

Conflict of Interest

The authors declare no conflict of interest.

Data Availability Statement

The data that support the findings of this study are available from the corresponding author upon reasonable request.

Keywords

generalized vortices, geometric phase, metasurfaces, near-field, orbital angular momentum

Received: May 27, 2022

Revised: July 16, 2022

Published online:

- [1] L. Allen, M. W. Beijersbergen, R. J. C. Spreeuw, J. P. Woerdman, *Phys. Rev. A* **1992**, *45*, 8185.
- [2] Q. Zhan, *Adv. Opt. Photonics* **2009**, *1*, 1.
- [3] J. Wang, J. Y. Yang, I. M. Fazal, N. Ahmed, Y. Yan, H. Huang, Y. Ren, Y. Yue, S. Dolinar, M. Tur, *Nat. Photonics* **2012**, *6*, 488.
- [4] Y. Yan, G. D. Xie, M. P. J. Lavery, H. Huang, N. Ahmed, C. G. Bao, Y. X. Ren, Y. W. Cao, L. Li, Z. Zhao, A. F. Molisch, M. Tur, M. J. Padgett, A. E. Willner, *Nat. Commun.* **2014**, *5*, 4876.
- [5] M. Padgett, R. Bowman, *Nat. Photonics* **2011**, *5*, 343.
- [6] J. Chu, D. Chu, Q. Smithwick, *Research* **2019**, 2019, 9564593.
- [7] T. Stav, A. Faerman, E. Maguid, D. Oren, V. Kleiner, E. Hasman, M. Segev, *Science* **2018**, *361*, 1101.
- [8] N. Gao, C. Q. Xie, *Opt. Lett.* **2012**, *37*, 3255.
- [9] J. M. Hickmann, E. J. S. Fonseca, W. C. Soares, S. Chávez-Cerda, *Phys. Rev. Lett.* **2010**, *105*, 053904.
- [10] D. Novoa, I. J. Sola, M. A. Garcia-March, A. Ferrando, *Appl. Phys. B* **2014**, *116*, 779.
- [11] N. F. Yu, P. Genevet, M. A. Kats, F. Aieta, J. P. Tetienne, F. Capasso, Z. Gaburro, *Science* **2011**, *334*, 333.
- [12] L. L. Huang, X. Z. Chen, H. Mühlenbernd, G. X. Li, B. F. Bai, Q. F. Tan, G. F. Jin, T. Zentgraf, S. Zhang, *Nano Lett.* **2012**, *12*, 5750.
- [13] X. F. Zang, B. S. Yao, L. Chen, J. Y. Xie, X. G. Guo, A. V. Balakin, A. P. Shkurinov, S. L. Zhuang, *Light Adv. Manufact.* **2021**, *2*, 10.
- [14] X. J. Ni, N. K. Emani, A. V. Kildishev, A. Boltasseva, V. M. Shalaev, *Science* **2012**, *335*, 427.
- [15] L. X. Liu, X. Q. Zhang, M. Kenney, X. Q. Sun, N. N. Xu, C. M. Ouyang, Y. L. Shi, J. G. Han, W. L. Zhang, S. Zhang, *Adv. Mater.* **2015**, *26*, 5031.
- [16] Z. C. Liu, Z. C. Li, Z. Liu, J. X. Li, H. Cheng, P. Yu, W. W. Liu, C. C. Tang, C. Z. Gu, J. J. Li, S. Q. Chen, J. G. Tian, *Adv. Fun. Mater.* **2015**, *25*, 5428.
- [17] X. J. Ni, A. V. Kildishev, V. M. Shalaev, M. Vladimir, *Nat. Commun.* **2013**, *4*, 2807.
- [18] Y. Yifat, M. Eitan, Z. Iluz, Y. Hanein, A. Boag, J. Scheuer, *Nano Lett.* **2014**, *14*, 2485.
- [19] G. X. Zheng, H. Mühlenbernd, M. Kenney, G. X. Li, T. Zentgraf, S. Zhang, *Nat. Nanotechnol.* **2015**, *10*, 30812.
- [20] D. D. Wen, F. Y. Yue, G. X. Li, G. X. Zheng, K. L. Chan, S. M. Chen, M. Chen, K. F. Li, P. W. H. Wong, K. W. Cheah, E. Y. B. Pun, S. Zhang, X. Z. Chen, *Nat. Commun.* **2015**, *6*, 1.
- [21] Q. Xu, X. Q. Zhang, Y. H. Xu, C. M. Ouyang, Z. Tian, J. Q. Gu, J. Li, S. Zhang, J. G. Han, W. L. Zhang, *Laser Photonics Rev.* **2017**, *11*, 1600212.
- [22] L. Jin, Z. G. Dong, S. T. Mei, Y. F. Yu, Z. Wei, Z. Y. Pan, S. D. Rezaei, X. P. Li, A. I. Kuznetsov, Y. S. Kivshar, J. K. W. Yang, C.-W. Qiu, *Nano Lett.* **2018**, *18*, 8016.
- [23] Y. Wang, C. S. Guan, H. Y. Li, X. M. Ding, K. Zhang, J. X. Wang, S. N. Burokur, J. Liu, Q. Wu, *Adv. Photon. Res.* **2020**, *1*, 2000022.
- [24] I. Kim, J. Jang, G. Kim, J. Lee, T. Badloe, J. Mun, J. Rho, *Nat. Commun.* **2021**, *12*, 3614.
- [25] X. Z. Chen, L. L. Huang, H. Mühlenbernd, G. X. Li, B. F. Bai, Q. F. Tan, G. F. Jin, C.-W. Qiu, S. Zhang, T. Zentgraf, *Nat. Commun.* **2012**, *3*, 1.
- [26] X. Z. Chen, M. Chen, M. Q. Mehmood, D. D. Wen, F. Y. Yue, C.-W. Qiu, S. Zhang, *Adv. Opt. Mater.* **2015**, *3*, 1201.
- [27] A. Arbabi, Y. Horie, M. Bagheri, A. Faraon, *Nat. Nanotechnol.* **2015**, *10*, 937.
- [28] M. Khorasaninejad, W. T. Chen, R. C. Devlin, J. Oh, A. Y. Zhu, F. Capasso, *Science* **2016**, *352*, 1190.
- [29] R. J. Lin, V.-C. Su, S. M. Wang, M. K. Chen, T. L. Chung, Y. H. Chen, H. Y. Kuo, J.-W. Chen, J. Chen, Y. T. Huang, J.-H. Wang, C. H. Chu, P. C. Wu, T. Li, Z. L. Wang, S. N. Zhu, D. P. Tsai, *Nat. Nanotechnol.* **2018**, *14*, 227.
- [30] S. M. Wang, P. C. Wu, V.-C. Su, Y.-C. Lai, M. K. Chen, H. Y. Kuo, B. H. Chen, Y. H. Chen, T.-T. Huang, J.-H. Wang, R.-M. Lin, C.-H. Kuan, T. Li, Z. L. Wang, S. N. Zhu, D. P. Tsai, *Nat. Nanotechnol.* **2018**, *13*, 227.
- [31] W. T. Chen, A. Y. Zhu, V. Sanjeev, M. Khorasaninejad, Z. J. Shi, E. Lee, F. Capasso, *Nat. Nanotechnol.* **2019**, *13*, 220.
- [32] X. F. Zang, H. Z. Ding, Y. Intaravanne, L. Chen, Y. Peng, J. Y. Xie, Q. H. Ke, A. V. Balakin, A. P. Shkurinov, X. Z. Chen, Y. M. Zhu, S. L. Zhuang, *Laser Photonics Rev.* **2019**, *13*, 1900182.
- [33] X. F. Zang, W. W. Xu, M. Gu, B. S. Yao, L. Chen, Y. Peng, J. Y. Xie, A. V. Balakin, A. P. Shkurinov, Y. M. Zhu, S. L. Zhuang, *Adv. Opt. Mater.* **2020**, *8*, 1901342.
- [34] R. X. Wang, Y. Intaravanne, S. T. Li, J. Han, S. M. Chen, J. L. Liu, S. Zhang, L. Li, X. Z. Chen, *Nano Lett.* **2021**, *21*, 2081.
- [35] X. B. Yin, Z. L. Ye, J. Rho, Y. Wang, X. Zhang, *Science* **2013**, *339*, 1405.
- [36] X. H. Ling, X. X. Zhou, X. N. Yi, W. X. Shu, Y. C. Liu, S. Z. Chen, H. L. Luo, S. C. We, D. Y. Fan, *Light Sci. Appl.* **2015**, *4*, e290.
- [37] W. J. Luo, S. Y. Xiao, Q. He, S. L. Sun, L. Zhou, *Adv. Opt. Mater.* **2015**, *3*, 1102.
- [38] X. F. Zang, B. S. Yao, Z. Li, Y. Zhu, J. Y. Xie, L. Chen, A. V. Balakin, A. P. Shkurinov, Y. M. Zhu, S. L. Zhuang, *Nanophotonics* **2020**, *9*, 1501.
- [39] N. K. Grady, J. E. Heyes, D. R. Chowdhury, Y. Zeng, M. T. Reiten, A. K. Azad, A. J. Taylor, D. A. R. Dalvit, H. T. Chen, *Science* **2013**, *340*, 1304.
- [40] N. Yu, F. Aieta, P. Genevet, M. A. Kats, Z. Gaburro, F. Capasso, *Nano Lett.* **2012**, *12*, 6328.
- [41] R. H. Fan, Y. Zhou, X. P. Ren, R. W. Peng, S. C. Jiang, D. H. Xu, X. Xiong, X. R. Huang, M. Wang, *Adv. Mater.* **2015**, *27*, 1201.
- [42] X. F. Zang, H. H. Gong, Z. Li, J. Y. Xie, Q. Q. Cheng, L. Chen, A. P. Shkurinov, Y. M. Zhu, S. L. Zhuang, *Appl. Phys. Lett.* **2018**, *112*, 171111.
- [43] S. Wang, Z. L. Deng, Y. J. Wang, Q. B. Zhou, X. L. Wang, Y. Y. Cao, B. O. Guan, S. M. Xiao, X. P. Li, *Light Sci. Appl.* **2021**, *10*, 24.
- [44] G. X. Li, S. M. Chen, N. Pholchai, B. Reineke, P. W. H. Wong, E. Y. B. Pun, K. W. Cheah, T. Zentgraf, S. Zhang, *Nat. Mater.* **2015**, *14*, 607.
- [45] E. Almeida, O. Bitto, Y. Prior, *Nat. Commun.* **2016**, *7*, 12533.
- [46] F. Walter, G. X. Li, C. Meier, S. Zhang, T. Zentgraf, *Nano Lett.* **2017**, *17*, 3171.
- [47] M. L. Ma, Z. Li, W. W. Liu, C. C. Tang, Z. C. Li, H. Cheng, J. J. Li, S. Q. Chen, J. G. Tian, *Laser Photon. Rev.* **2019**, *13*, 1900045.
- [48] Y. M. Yang, W. Y. Wang, P. Moitra, I. I. Kravchenko, D. P. Briggs, J. Valentine, *Nano Lett.* **2014**, *14*, 1394.
- [49] H. Cheng, Z. C. Liu, S. Q. Chen, J. G. Tian, *Adv. Mater.* **2015**, *27*, 5410.
- [50] E. Maguid, I. Yulevich, D. Veksler, V. Kleiner, M. L. Brongersma, E. Hasman, *Science* **2016**, *352*, 1202.
- [51] X. F. Zang, Y. M. Zhu, C. X. Mao, W. W. Xu, H. Z. Ding, J. Y. Xie, Q. Q. Cheng, L. Chen, Y. Peng, Q. Hu, M. Gu, S. L. Zhuang, *Adv. Opt. Mater.* **2018**, *7*, 1801328.
- [52] K. Zhang, Y. Y. Yuan, X. M. Ding, H. Y. Li, B. Ratni, Q. Wu, J. Liu, S. N. Burokur, J. B. Tan, *Laser Photon. Rev.* **2020**, *15*, 2000351.
- [53] F. Y. Yue, D. D. Wen, C. M. Zhang, B. D. Gerardot, W. Wang, S. Zhang, X. Z. Chen, *Adv. Mater.* **2017**, *29*, 1603838.
- [54] Y. J. Bao, J. C. Ni, C. W. Qiu, *Adv. Mater.* **2020**, *32*, 1905659.
- [55] J. Han, Y. Intaravanne, A. Ma, R. X. Wang, S. T. Li, Z. C. Li, S. Q. Chen, J. S. Li, X. Z. Chen, *Laser Photon. Rev.* **2020**, *14*, 2000146.
- [56] M. Z. Liu, P. C. Huo, Q. Zhu, C. Zhang, S. Zhang, M. W. Song, S. Zhang, Q. W. Zhou, L. Chen, H. J. Lezec, A. Agrawal, Y. Q. Lu, T. Xu, *Nat. Commun.* **2021**, *12*, 2230.
- [57] J. F. Xie, H. M. Guo, S. L. Zhuang, J. B. Hu, *Opt. Express.* **2021**, *29*, 3081.
- [58] Y. C. Zhang, J. Gao, X. D. Yang, *Adv. Opt. Mater.* **2019**, *7*, 1901152.

- [59] X. Zhang, L. L. Huang, R. Z. Zhao, Q. S. Wei, X. Li, G. Z. Geng, J. J. Li, X. W. Li, Y. T. Wang, S. Zhang, *Laser Photon. Rev.* **2022**, *16*, 2100451.
- [60] G. Spektor, D. Kilbane, A. K. Mahro, B. Frank, S. Ristok, L. Gal, P. Kahl, D. Podbiel, S. Mathias, H. Giessen, F.-J. M. Z. Heringdorf, M. Orenstein, M. Aeschlimann, *Science* **2017**, *355*, 1187.
- [61] B. Frank, P. Kahl, D. Podbiel, G. Spektor, M. Orenstein, L. W. Fu, T. Weiss, M. H.-V. Hoegen, T. J. Davis, F.-J. M. Z. Heringdorf, H. Giessen, *Sci. Adv.* **2017**, *3*, 700721.
- [62] Y. Meng, Y. Z. Chen, L. H. Lu, Y. M. Ding, A. Cusano, J. A. Fan, Q. M. Hu, K. Y. Wang, Z. W. Xie, Z. T. Liu, Y. M. Yang, Q. Liu, M. L. Gong, Q. R. Xiao, S. L. Sun, M. M. Zhang, X. C. Yuan, X. J. Ni, *Light Sci. Appl.* **2021**, *10*, 235.
- [63] J. Lin, J. P. B. Mueller, Q. Wang, G. H. Yuan, N. Antoniou, X. C. Yuan, F. Capasso, *Science* **2013**, *340*, 331.
- [64] S. Y. Lee, S. J. Kim, H. Kwon, B. Lee, *IEEE Photon. Technol. Lett.* **2015**, *27*, 705.